

Imaging Renal Urea Handling in Rats at Millimeter Resolution Using Hyperpolarized Magnetic Resonance Relaxometry

Galen D. Reed^{1,2}, Cornelius von Morze¹, Alan S. Verkman³, Bertram L. Koelsch^{1,2}, Myriam M. Chaumeil¹, Michael Lustig^{2,4}, Sabrina M. Ronen^{1,2}, Robert A. Bok¹, Jeff M. Sands⁵, Peder E. Z. Larson^{1,2}, Zhen J. Wang¹, Jan Henrik Ardenkjær Larsen^{6,7}, John Kurhanewicz^{1,2}, and Daniel B. Vigneron^{1,2}

¹Department of Radiology and Biomedical Imaging, University of California, San Francisco, San Francisco, California; ²Graduate Group in Bioengineering, University of California San Francisco, San Francisco, California, and University of California Berkeley, Berkeley, California; ³Departments of Medicine and Physiology, University of California San Francisco, San Francisco, California; ⁴Department of Electrical Engineering and Computer Sciences, University of California Berkeley, Berkeley, California; ⁵Department of Medicine, Renal Division, Emory University, Atlanta, Georgia; and ⁶GE Healthcare, Brøndby, Denmark; and ⁷Department of Electrical Engineering, Technical University of Denmark, Kongens Lyngby, Denmark

Corresponding Author:

Galen Reed

Byers Hall Suite 102, MC 2512, San Francisco, CA, 94158-2330;

E-mail: galen.d.reed@gmail.com

Key Words: urea, dynamic nuclear polarization, NMR relaxation, transporter

Abbreviations: Urea transporters (UT), inner medullary collecting ducts (IMCD), magnetic resonance imaging (MRI), gadolinium (Gd), inner medulla (IM), Hyperpolarized bis-1,1-(hydroxymethyl)-1-¹³C-cyclopropane-²H₈ (HMPC), glomerular filtration rate (GFR), Bovine serum albumin (BSA), Gd/diethylenetriaminepentaacetic acid (GdDTPA), field of view (FOV), repetition time (TR), echo time (TE), signal-to-noise ratio (SNR), outer stripe of the outer medulla (OSOM), inner stripe of the outer medulla (ISOM)

ABSTRACT

In this study, *in vivo* T2 heterogeneity of hyperpolarized [¹³C, ¹⁵N₂]urea in rat kidney has been investigated. Selective quenching of the vascular hyperpolarized ¹³C signal with a macromolecular relaxation agent revealed that a long T2 component of the [¹³C, ¹⁵N₂]urea signal originated from the renal extravascular space, thus allowing the vascular and renal filtrate contrast agent pools of the [¹³C, ¹⁵N₂]urea to be distinguished via multiexponential analysis. The T2 response to induced diuresis and antidiuresis was determined using 2 imaging agents—hyperpolarized [¹³C, ¹⁵N₂]urea and hyperpolarized bis-1,1-(hydroxymethyl)-1-¹³C-cyclopropane-²H₈ (control agent). During antidiuresis, large T2 increases in the inner medulla and papilla were observed using the former agent only. Therefore, [¹³C, ¹⁵N₂]urea relaxometry is sensitive to the following 2 steps of the renal urea handling process: glomerular filtration process and inner medullary urea transporter-A1- and urea transporter-A3-mediated urea concentrating process. To aid multiexponential data analysis, simple motion correction and subspace denoising algorithms are presented. Furthermore, a T2-edited, ultralong echo time sequence was developed for sub-2 mm³ resolution 3-dimensional encoding of urea by exploiting relaxation differences in the vascular and filtrate pools.

INTRODUCTION

Urea is the primary end product of nitrogen metabolism in mammals, and humans typically produce more than 20 g of urea per day (1). One of the primary functions of the mammalian kidney is concentrating urea to >100 times plasma levels for efficient excretion of this large osmotic load while minimizing water loss (2-5). Renal urea handling is a multistep process beginning with filtration of blood at the glomerulus followed by a countercurrent multiplication in the medulla. The countercurrent exchange is assisted by urea transporters (UTs) expressed in the descending thin limb of the loops of Henle (UT-A2 isoform), in erythrocytes (UT-B isoform), and in the inner 2/3 of the inner medullary collecting ducts (IMCD; UT-A1 and UT-A3 isoforms) (4-7). The IMCD transporters UT-A1 and UT-A3 increase the

effective permeability of the tubular wall in the presence of vasopressin, thus allowing urea to freely pass into the inner medullary interstitial fluid where it can accumulate to >1M concentration when water conservation is important.

Imaging renal solute handling could be a potentially valuable tool for the study of renal function. Several magnetic resonance imaging (MRI) studies have shown noninvasive sodium imaging using (23) Na-detected MRI (8, 9). Indirect urea detection via changes in the ¹H water resonance after radio frequency saturation of the urea amide frequency has been shown (10). Recently, direct MRI of intravenously injected ¹³C-labeled urea (11-15) and numerous other small molecules (16-26) has been enabled using dynamic nuclear polarization (27). In this process, the isotopically enriched molecule is doped

with an organic radical, cooled to liquid helium temperatures, and irradiated at microwave frequencies to achieve polarizations many orders of magnitude above thermal equilibrium values. After dissolution, the polarization decays exponentially with a time constant T_1 which is typically 10–90 seconds for ^{13}C -labeled carbonyl sites (28, 18). This method has been used to generate background-free angiograms in preclinical models using highly biocompatible contrast agents (11, 29).

The current study further investigates the physiological significance of hyperpolarized ^{13}C renal urea relaxation times by linking these measurements to underlying steps of the urea handling process. In a prior study, ^{13}C -detected hyperpolarized [^{13}C , $^{15}\text{N}_2$]urea T2 mapping experiments performed in Sprague–Dawley rats gave uniform urea T2 values of ~1 second throughout in the animal with the exception of the kidneys, where values between 4 and 15 seconds were noted (30). However, it remained unclear whether these long T2 signals originated from the renal vasculature, from within the tubular lumen, from the medullary interstitium, or some combination of these. In the first set of experiments presented here, a chase infusion of an intravascular macromolecular relaxation agent was performed after hyperpolarized [^{13}C , $^{15}\text{N}_2$]urea injection but before T2 measurement. The gadolinium (Gd) chelates attached to the macromolecular complex substantially shortened the spin-lattice relaxation time of the hyperpolarized [^{13}C , $^{15}\text{N}_2$]urea, thereby rapidly reducing its polarization and diminishing its signal. However, the macromolecular carrier restricts this effect to the vascular space. Therefore, the attenuation of the short and long T2 signals (compared with T2 measurements performed without the macromolecular relaxation agent in the control group) indicated whether the renal vasculature contributed to the long T2 signal. The second set of experiments investigated the hyperpolarized [^{13}C , $^{15}\text{N}_2$]urea T2 response to rats on induced antidiuresis. Prior experiments showed greater centralization of the hyperpolarized urea signal in the kidney in the rats on induced antidiuresis (12). In the antidiuresis state, the kidneys are in water conservation mode, and the inner medullary transporters UT-A1 and UT-A3 aid to maximally concentrate urea in the inner medulla (IM). During the osmotic diuresis state, low levels of circulating vasopressin and reduced UT-A1 and UT-A3 activity imply that urea excretion will be largely mediated by passive membrane diffusion (31). The experiments performed in this study more definitively attribute this effect to the UT-A1 and UT-A3 by comparing measurements of hyperpolarized [^{13}C , $^{15}\text{N}_2$]urea T2 to those of a control molecule. Hyperpolarized bis-1,1-(hydroxymethyl)-1- ^{13}C -cyclopropane- $^2\text{H}_8$ (commonly abbreviated as HMCP or HP001) served as this control because it is nonendogenous and has no specific renal transport mechanisms aside from passive diffusion and tubular flow. The use of this control agent aids the accountability of the potential relaxation time changes due to transient glomerular filtration rate (GFR) changes or hydration status. To facilitate all relaxometry measurements, an alignment algorithm was created for the compensation of respiratory motion throughout image acquisition. A subspace denoising combined with a regularized estimation algorithm addressed the inherent difficulty and noise amplification inherent in multiexponential analysis. Finally, an additional T2-edited, high isotropic (<2 mm³) resolution imaging

sequence was shown as a potential method of discriminating the short T2 vascular and long T2 filtrate pools.

METHODOLOGY

Animal Handling

Animal studies were performed under a protocol approved by the University of California San Francisco's Institutional Animal Care and Utilization Committee. Sprague–Dawley rats (mean mass, 400 g) were anesthetized with a 1.7% isoflurane/oxygen mixture under a constant flow rate of 1 L/min. Animals were imaged in the supine position inside the birdcage coil and thermally insulated via heat pad. Contrast agents were injected via lateral tail vein catheters. Rats were housed 3 per cage at the University of California San Francisco's Laboratory Animal Resource Center.


Hardware

Imaging experiments were conducted in a GE 3 T clinical MRI (GE Medical Systems, Waukesha, Wisconsin) equipped with a rat-sized dual-tuned $^1\text{H}/^{13}\text{C}$ transceiver birdcage radio frequency coil (8 cm inner diameter) placed on the patient table. A HyperSense polarizer (Oxford Instruments, Oxford, UK) was used for dissolution dynamic nuclear polarization experiments.

Sample Preparation

Isotopically enriched [^{13}C , $^{15}\text{N}_2$]urea and bis-1,1-(hydroxymethyl)-1- ^{13}C -cyclopropane- $^2\text{H}_8$ were each doped with the trityl radical OX063 (Oxford Instruments) and Dotarem (Guerbet, Roissy, France) as previously described (30, 21, 32). Supplementary urea ^{15}N labeling was necessary for the T2 increase afforded by the elimination of the scalar coupling of the second kind of relaxation pathway (33, 30). Bovine serum albumin (BSA) conjugated with an average of 23 Gd/diethylenetriaminepentaacetic acid (GdDTPA) chelates per BSA molecule (abbreviated as BSA-GdDTPA; molecular weight, ~85 kDa) was synthesized using methods previously described (34, 35).

^{13}C MRI Acquisition

T2 Mapping. ^{13}C T2 mapping was performed using sequences previously described (30). Dynamic projection images were acquired in the coronal plane with 1 mm of in-plane resolution, 14 × 7 cm of field of view (FOV), 13 milliseconds of repetition time (TR), and 70 phase encodes per image, giving a temporal resolution of 910 milliseconds and total acquisition time of 18.2 seconds for all 20 echoes. Images were reconstructed with a simple 2-dimensional Fourier transform without spatial filtering. After reconstruction, some first-time-point images suffered from receiver over-ranging (Supplemental Video 4 ). These images were excluded, and an analysis was performed on the subsequent time points.

Relaxometric Data Analysis

Motion Correction. Periodic respiratory motion caused a 1–2 mm offset, which was largely resolved along the superior/inferior axis of the animal. To correct this observed shift, a simple search algorithm was developed, in which each image was aligned with its previous time point. Given that the motion was primarily 1-dimensional, a brute-force search was implemented, which translated each image in 1 mm increments over ±1 cm

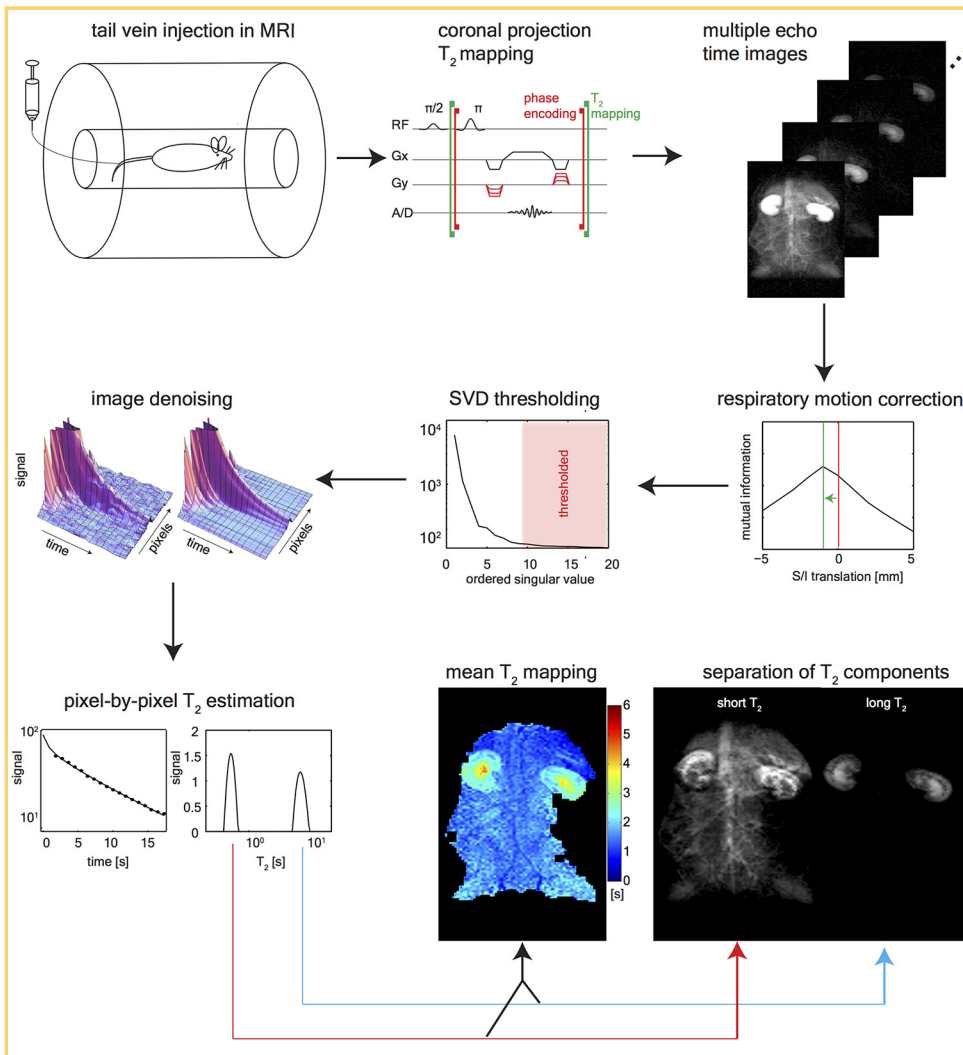


Figure 1. Hyperpolarized ^{13}C T₂ mapping methodology. Hyperpolarized ^{13}C -labeled substrates were injected via lateral tail vein catheter inside the magnetic resonance imaging (MRI) scanner. The T₂ mapping sequence acquired coronal projection images at 0.9 seconds echo time (TE) intervals while playing 180° pulses for 18 seconds. Each image is then corrected for respiratory motion via rigid translation in the superior/inferior direction. The dynamic images are then denoised using a singular value decomposition (SVD)-based thresholding in the space/time dimensions. The signal component at each T₂ is estimated using a regularized version of the T₂ nonnegative least squares method, and the long and short T₂ signal components are isolated by integrating the T₂ distribution.

from the initial location along the superior/inferior axis (for a total of 20 sampling points). At each position, the normalized mutual information was calculated between the floating image and the previous time point, thus generating an mutual information versus translation curve as shown in Figure 1. The shift that maximized this curve was then applied. An example of the motion-corrected images can be seen in Supplemental Video 1 [PLAY VIDEO](#).

Subspace Denoising. Outside of the kidneys, the majority of the ^{13}C signal disappeared after the first few echoes (Figure 1). This led to low-rank data matrices in the spatiotemporal dimensions. Therefore, a singular value decomposition-based denoising (36) could be used to better condition the ill-posed problem of multiexponential estimation (37–40). The 3-dimensional (3D) images (x, y, t) were concatenated along the x and y dimensions forming the matrix $I(r, t)$. Singular values less than the largest 7 (out of 20) were set to 0. This singular value decomposition-thresholded matrix was then used for the regularized T₂ estimation (Figure 1).

Multi-Exponential Analysis. The T₂ nonnegative least squares algorithm (38) was used for quantitative analysis of the time-decay data. This method uses a least squares inversion with nonnegativity constraints to estimate $s(\text{T}_2)$, the signal's T₂ distribution at each pixel. The T₂ nonnegative least squares is appealing, as it requires no *a priori* assumptions on the number of decay modes. However, regularization, necessary for the

management of noise amplification, imposes assumptions of the shape of the distribution. L_2 norm regularization smoothly produces varying distributions, whereas L_1 norm regularization generates a sparse T₂ spectra (38). We observed similar image appearance when using L_1 - and L_2 -regularized inversion of separation of short and long T₂ signal components, but the sparse T₂ spectra were easier to interpret visually (Figure 3D). The inverse problem with L_1 constraints was minimized as follows:

$$\|As - y\|^2 + \lambda \|s\|_1, \quad (1)$$

where matrix A has the following elements:

$$A_{ij} = e^{-t_j/T_{2,i}}. \quad (2)$$

$T_{2,i}$ is an array of 128 logarithmically spaced T₂ values ranging from 3 to 20 seconds, t_j is the echo time (TE; 20 regularly spaced from 0.5 to 19 seconds), and y_j is the detected pixel signal-to-noise ratio (SNR) values of the j th echo. The regularization parameter λ was chosen to be 0.01% of λ_{\max} , where λ_{\max} is the maximum possible value for which the solution is nonzero: $\lambda_{\max} = 2\max(A^T Y)$ (41).

From the distribution of $s(\text{T}_2)$, the signal $S_{\alpha,\beta}$ in the range $T_2 \in [\alpha, \beta]$ was calculated by integrating the $s(\text{T}_2)$ from α to β . A mean (T_2) measure in the range of $T_2 \in [\alpha, \beta]$ was estimated by the first moment of the distribution:

$$\langle T_2 \rangle = \exp \left\{ \frac{\int_{\alpha}^{\beta} s(T_2) \log T_2 dT_2}{\int_{\alpha}^{\beta} s(T_2) dT_2} \right\}. \quad (3)$$

The integration limits α and β were used to isolate short or long T2 species.

¹³C Urea/BSA-GdDTPA Relaxometry

¹³C Imaging Experiments. These experiments were designed to selectively quench the vascular ¹³C urea polarization while measuring the differential attenuation of the short and long T2 signal components. Analogous to previously reported experiments (42), a Gd carrier molecule was infused after the hyperpolarized ¹³C injection but before ¹³C detection. The paramagnetic Gd greatly reduces the T1 of the ¹³C molecule, thus causing rapid ¹³C polarization loss in regions where the ¹³C-labeled molecule and the Gd carrier are in proximity. This polarization loss manifests as a decreased signal during ¹³C imaging. This study used BSA as the carrier, which was conjugated with an average of 23 GdDTPA per BSA. This well-characterized blood pool agent has a high molecular weight (85 kDa) that prohibits extravasation and glomerular filtration on the subminute time-scale (34, 35).

To estimate the efficacy of hyperpolarized ¹³C signal quenching, the ¹³C T1 relaxivity of [¹³C,¹⁵N₂]urea with respect to BSA-GdDTPA was measured. BSA-GdDTPA was titrated in ~0.2mM increments into a 1-mL vial containing 1M [¹³C,¹⁵N₂]urea. At each titration point, the ¹³C urea T1 was measured via saturation recovery experiments at $B_0 = 3 \text{ T}$, $T = 27^\circ\text{C}$. A linear fit was performed on the [BSA-GdDTPA] versus 1/T1 data points. Using this measured curve in conjunction with model-based estimates of the rats' blood volumes (43), the in vivo T1 of ¹³C urea within the blood pool was roughly estimated.

In this study, 4 rats were imaged after 2 separate ¹³C urea injections: 1 with the BSA-GdDTPA chaser and 1 without to act as the control experiment. Because of the persistence of the BSA-GdDTPA in the blood pool, the chaser experiment was always performed after the control. Figure 3A shows a schematic of the experimental timeline. Rats were injected with 3 mL, 150mM hyperpolarized [¹³C,¹⁵N₂]urea solution over 12 seconds. The hyperpolarized urea was then allowed to diffuse for 28 seconds, and the ¹³C T2 mapping sequence was initiated 40 seconds after the beginning of injection; 2 hours later, a second [¹³C,¹⁵N₂]urea infusion was performed over 12 seconds. The hyperpolarized urea was then allowed to diffuse for 20 seconds, then 1 mL, 0.59mM BSA-GdDTPA (15mM GdDTPA) was injected over 1 second. The chaser was allowed to diffuse for 7 seconds, and then the ¹³C T2 mapping sequence was initiated again 40 seconds after the beginning of the urea injection.

Data Analysis. Image noise was estimated by the standard deviation of a signal-free region of the ¹³C images (before image denoising), and all image pixels were normalized by this measurement. Pixels with first-time-point-SNR of >10 were included in the analysis. Multiexponential estimation [equation (1)] was performed pixel-wise after image alignment and denoising. After calculation of $s(T_2)$, the short and long T2 signal components were isolated from the T2 distributions calculated at each pixel using the integration limits ($\alpha = 0.3$ seconds, $\beta = 2.5$ seconds) for the short T2 component and ($\alpha = 2.5$ seconds, $\beta = 20$ seconds) for the long T2 component. After separation of the short and long T2 signal components, the following metrics were compared: SNR, mean T2 [from equation (3) with the same

integration limits], and total number of pixels with SNR >10, giving a total of 6 metrics for each animal. Mean values of SNR and T2 were computed from within manually delineated kidney margins for each animal. Each metric was compared via non-parametric Wilcoxon rank-sum test between the [¹³C,¹⁵N₂]urea + BSA-GdDTPA experiments and control [¹³C,¹⁵N₂]urea experiments. $P < .05$ was used as the significance criteria. In addition, all pixels from the short T2 and long T2 maps from all 4 animals were binned by SNR and plotted on top of each other as an aid for visualizing the BSA-GdDTPA chaser effects.

¹H MRI. For qualitative visualization of the Gd carrier distribution, ¹H-detected, T1-weighted images were acquired 5 minutes post infusion of BSA-GdDTPA. This was followed by an additional injection of 1 mL, 0.5mM low molecular weight (940 Da) Gd-DTPA without attached albumin (Magnevist, Bayer Schering, Berlin). Both Gd agents were imaged with the same ¹H spoiled gradient echo sequence (flip angle = 35, TE/TR = 1.4/7 milliseconds, 3 averages, 0.8 mm isotropic resolution).

Diuresis/Antidiuresis Relaxometry

¹³C Imaging Experiments. The T2 response of hyperpolarized [¹³C,¹⁵N₂]urea and the control molecule hyperpolarized ¹³C HMCP to induced antidiuresis and osmotic diuresis in rats was measured. The methods for inducing diuresis and antidiuresis were identical to those described previously (12). For the antidiuresis protocol, the rats were deprived of food and water for an overnight period of 16 hours. To induce osmotic diuresis, the rats were first deprived of food and water for 16 hours and then allowed free access to aqueous glucose (10% by mass) solution for 9 hours. In each experiment, the urea (3 mL, 150mM hyperpolarized [¹³C,¹⁵N₂]urea) was injected at least 2 hours before the HMCP injection (3 mL, 125mM hyperpolarized HMCP). The T2 mapping sequence was initiated 40 seconds after the beginning of injection with identical acquisition parameters aside from a 4.5 kHz resonance frequency offset between urea and HMCP.

Data Analysis. A single mean (T_2) value was calculated at each pixel from the $s(T_2)$ distribution by calculating the first moment [equation (3)] over the full distribution ($\alpha = 0.3$ seconds, $\beta = 20$ seconds). Using the full distribution to compute a single (T_2) value simplified the comparison of 2 molecules with differing multiexponential T2 decay curves. Further, 4 maps were computed for each of the 3 animals: (T_2) maps for [¹³C,¹⁵N₂]urea and HMCP in diuresis and antidiuresis states. Histograms including all pixels binned by (T_2) were plotted for each agent to visualize the effect of diuresis and antidiuresis states.

For quantitative comparison, the cortex, outer stripe of the outer medulla (OSOM), inner stripe of the outer medulla (ISOM), and IM were delineated in ¹H localizer images. The (T_2) values from each of the 4 maps were then binned, and a mean value for each map was calculated for each animal. Paired statistical tests were performed in each kidney region for each ¹³C agent in diuresis and antidiuresis states using the Wilcoxon rank-sum test. $P < .05$ was used as the significance criteria.

¹H MRI. Animals were imaged in the coronal and axial planes using a T2-weighted ¹H fast spin echo sequence with TR = 1 second, TE = 100 milliseconds, 32 echoes, and 0.8-mm in-plane resolution.

T2-edited 3D imaging

The long TE MRI acquisition will filter out the short T2 signal components, and this may be used as an under-sampling

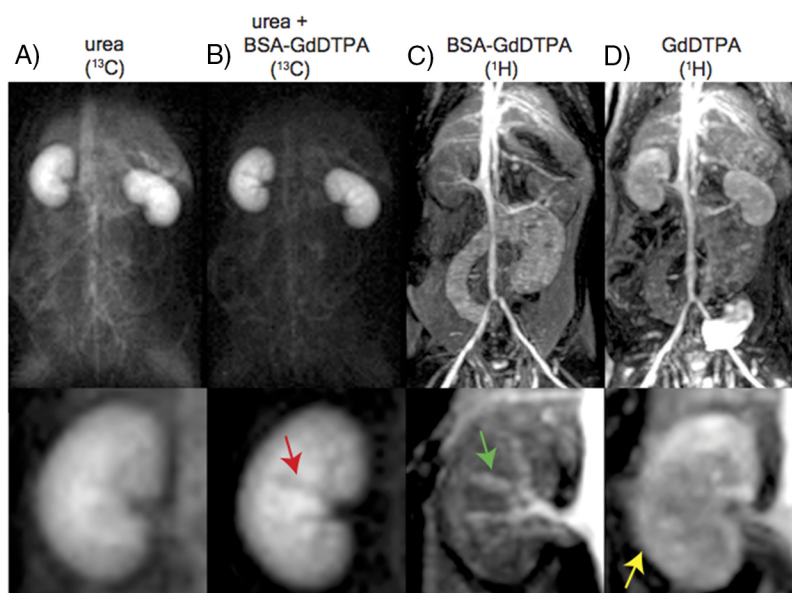


Figure 2. Attenuation of the hyperpolarized [^{13}C , $^{15}\text{N}_2$]urea signal is anatomically consistent with the macromolecular Gd carrier. Large field of view (FOV) images are shown on the top, and the bottom panels are zoomed to the kidney. First time-point ^{13}C urea MRI image (A). ^{13}C urea MRI acquired 8 seconds after bovine serum albumin-Gd/diethylenetriaminepentaacetic acid (BSA-GdDTPA) infusion shows strong suppression of the vascular signal and interlobular arteries (red arrow) (B). ^1H MRI acquired 5 minutes after BSA-GdDTPA infusion (C). The interlobular arteries show positive contrast in this image (green arrow) demonstrating that BSA-GdDTPA is confined to the vascular space on the imaging time scale. ^1H MRI acquired 5 minutes after GdDTPA infusion (D). In contrast to BSA-GdDTPA (mass ~ 85 kDa), GdDTPA (mass ~ 938 Da) is freely filtered at the glomerulus (yellow arrow).

method to reduce the total number of phase encodes for achieving a high-resolution image. A 3D steady-state free precession (SSFP) acquisition was initiated at 20, 25, and 30 seconds after the beginning of urea injection. This sequence used a large flip angle ($\theta = 120^\circ$) and an extremely long TE (3.5 seconds), allowing for editing out the vascular signal with enhancement of the long T2 filtrate. The unaliased FOV was chosen to cover only the kidneys in the 2 phase-encoded dimensions. Rasterized, linear phase encode ordering was used, so the TE was half the total acquisition duration. An acquisition matrix with size (42, 42, 14) was acquired over a (5,5,1.7) cm FOV in (L-R,S-I,A-P) coordinates, yielding a 1.2-mm isotropic pixel length. Further, 588 phase encodes were acquired with TR = 12 milliseconds for a total scan time of 7 seconds. A signal simulation adapted from Svensson et al. (21) was used to estimate the blood pool suppression for different ^{13}C relaxation times:

$$\text{SNR} = \frac{1}{\sqrt{N}} \sum_{n=1}^N \sin \frac{\theta}{2} \left[\left(E_1 \cos \frac{\theta}{2} \right)^2 + \left(E_2 \sin \frac{\theta}{2} \right)^2 \right]^{n/2}. \quad (4)$$

Here, θ is the flip angle, N is the number of phase encode steps, $E_1 = \exp(-TR/T_1)$, $E_2 = \exp(-TR/T_2)$, and TR is the repetition time.

RESULTS

^{13}C Urea/BSA-GdDTPA Relaxometry

The T1 relaxivity of the BSA-GdDTPA complex on [^{13}C , $^{15}\text{N}_2$]urea was estimated to be $77 \pm 10 \text{mM}^{-1}\text{s}^{-1}$ with respect to the BSA

carrier, or $3.1 \pm 0.4 \text{mM}^{-1}\text{s}^{-1}$ per GdDTPA chelate ($R^2 = 0.97$) from saturation recovery experiments. Figure 3A, right, shows the measured T1 relaxivity curve, with error bars indicating T1 measurement uncertainty from the intrinsic SNR. The estimated rat blood volume was $27 \pm 3 \text{mL}$ (43). Therefore, at the expected in vivo BSA-GdDTPA of $\sim 0.024 \text{mM}$, the urea T1 should be ~ 0.5 seconds. Although this calculation is extremely rough, as it ignores circulation or potentially differing relaxivity in vivo and in vitro, the 7-second delay should have been adequate for any hyperpolarized [^{13}C , $^{15}\text{N}_2$]urea to undergo several T1 time constants of decay, leading to large polarization losses when in contact with BSA-GdDTPA.

Figure 2 shows a first echo [^{13}C , $^{15}\text{N}_2$]urea image with (Figure 2A) and without (Figure 2B) the chaser injection of the macromolecular BSA-GdDTPA relaxation agent. This image shows a large suppression of the vascular [^{13}C , $^{15}\text{N}_2$]urea signal throughout, as well as darkening of the interlobular branches of the renal artery (Figure 2B). The darkening of the renal arterial branches indicates that the 7-second delay was adequate not only for bolus arrival of the BSA-GdDTPA to the kidneys but also for the BSA-GdDTPA to cause substantial [^{13}C , $^{15}\text{N}_2$]urea polarization loss. These same arterial branches show up bright in a T1-weighted ^1H image (Figure 2c). No renal perfusion was detected with the BSA-GdDTPA agent up to 5 minutes after initial infusion. In contrast, the post-GdDTPA image (Figure 2D) shows renal perfusion and bladder accumulation because this agent is freely filtered at the glomerulus (44).

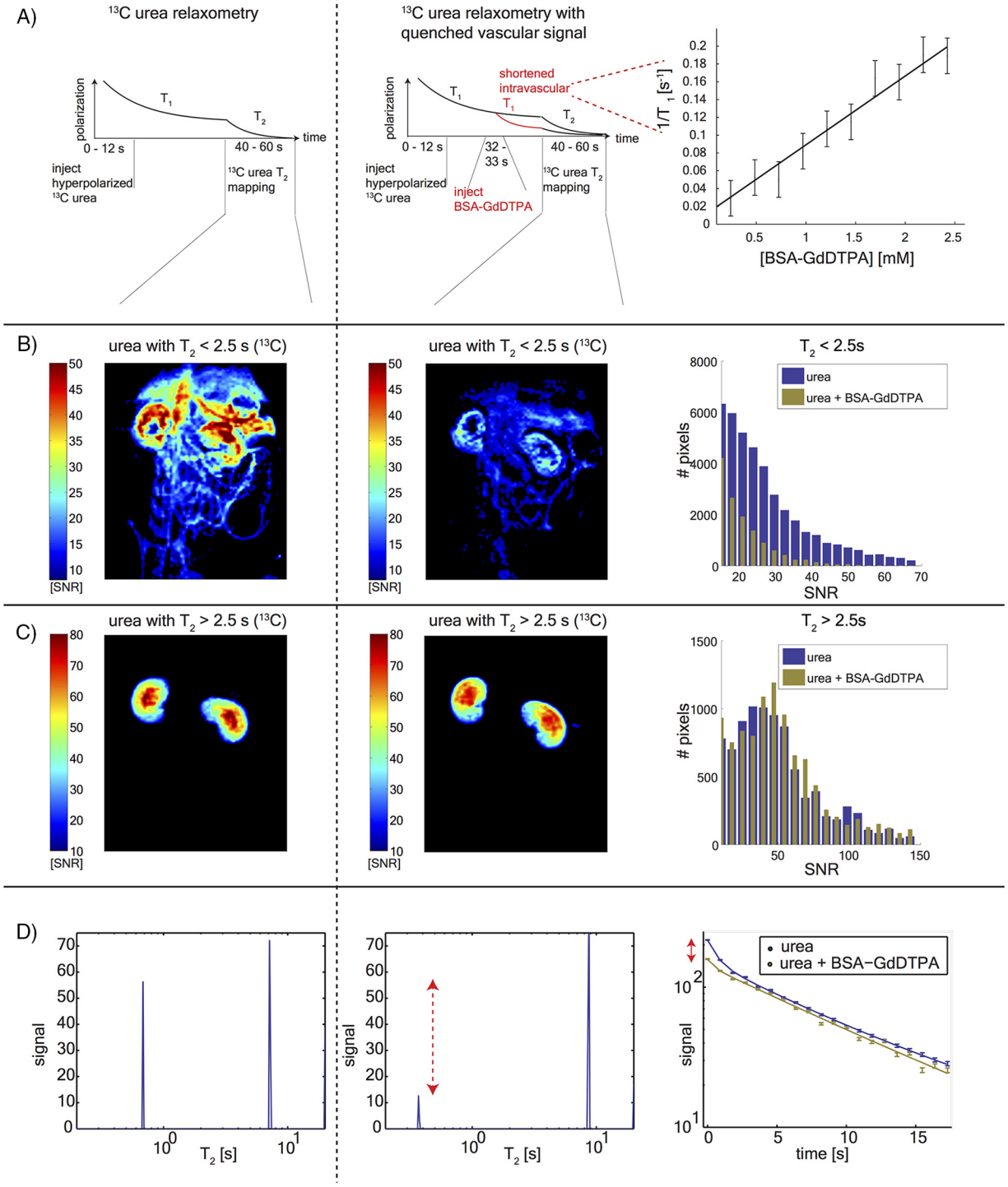


Figure 3. [^{13}C , $^{15}\text{N}_2$]urea T_2 relaxometry after quenching the vascular signal. Timeline of the substrate injections and imaging (A). The left column shows images from the control experiment, and the center column shows the post-BSA-GdDTPA images. The [^{13}C , $^{15}\text{N}_2$]urea T_1 /BSA-GdDTPA relaxivity curve is shown on the right. [^{13}C , $^{15}\text{N}_2$]urea signal outside of the kidneys has T_2 of < 2.5 seconds, which is strongly attenuated by BSA-GdDTPA (B). Pixel distributions from 4 animals are shown on the right. The long T_2 urea signal component is confined to the kidneys and is unaffected by the BSA-GdDTPA chaser (C). Pixel distributions from 4 animals are shown on the right. T_2 distributions of single pixels selected from the center of the kidneys are showing this short T_2 signal attenuation (red arrow) (D). Single-pixel T_2 decay curves (corresponding to the distributions in the left and center panels).

Table 1. ^{13}C urea T_2 Multiexponential Relaxometry after Quenching the Vascular Signal


	^{13}C , $^{15}\text{N}_2$ urea SNR [†]		^{13}C , $^{15}\text{N}_2$ urea (T_2) [s] [†]		Number of Pixels with SNR > 10 [‡]		n
	$T_2 < 2.5$ s	$T_2 > 2.5$ s	$T_2 < 2.5$ s	$T_2 > 2.5$ s	$T_2 < 2.5$ s	$T_2 > 2.5$ s	
^{13}C , $^{15}\text{N}_2$ urea	19.6 ± 4.3	41.2 ± 4.5	0.94 ± 0.05	6.07 ± 1.04	3500 ± 1000	570 ± 40	4
^{13}C , $^{15}\text{N}_2$ urea + BSA-GdDTPA*	12.4 ± 2.2	43.8 ± 2.9	0.76 ± 0.07	6.84 ± 1.50	1700 ± 1100	600 ± 100	4
p^{**}	0.029	0.343	0.029	0.200	0.114	0.886	

[†] Mean values within manually-delineated margins around the kidney.

[‡] Mean values over the entire animal.


* The ^{13}C urea/BSA-GdDTPA T_1 relaxivity was $77 \pm 10 \text{ mM}^{-1}\text{s}^{-1}$, or $3.1 \pm .4 \text{ mM}^{-1}\text{s}^{-1}$ per GdDTPA ($R^2 = .97$).

** Calculated via Wilcoxon rank sum test with data from the above two rows.


The dynamic ^{13}C , $^{15}\text{N}_2$ urea images acquired under T_2 decay conditions initially showed greatly reduced signal at early TE when accompanied by the BSA-GdDTPA chaser. At later TE, however, the images converge and look nearly identical. This effect is most easily visualized in Supplemental Video 2  as follows: by the seventh time point (corresponding to a 6.8-second TE), only urea within the kidneys is visible in both images, and the signal's spatial variation is nearly identical in the images with and without the BSA-GdDTPA chaser. The similarity persisted in all experiments until the end of imaging acquisition. At this TE, both images show urea signal throughout the cortex and medulla, and a dark rim is present at the OSOM. The later echo images were acquired up to 25 seconds after the infusion of the BSA-GdDTPA chaser and provide strong evidence that the slowly decaying ^{13}C , $^{15}\text{N}_2$ urea signal component emanated from regions inaccessible to the BSA-GdDTPA.

Multiexponential relaxometry quantified this dissimilarity at early echoes and similarity at late echoes. Figure 3, B and C show the short T_2 and long T_2 signal components, respectively, with the latter appearing identical in the ^{13}C , $^{15}\text{N}_2$ urea images with and without BSA-GdDTPA. Figure 3D shows a single decay curve from a pixel selected from the center of the kidney with semilog axes. The 2 decay modes show up as peaks in the T_2 distributions in Figure 3D, with the short T_2 component significantly reduced by the BSA-GdDTPA chaser. The SNR and T_2 measurements from all 4 animals is presented in Table 1. The BSA-GdDTPA chaser caused a significant reduction in the short T_2 SNR and T_2 values, with the latter indicating enhanced transverse relaxation of the macromolecular agent. Nonsignificant reductions were observed in the number of short T_2 pixels with SNR > 10. The long T_2 SNR was unaffected by the BSA-GdDTPA chaser, as was the mean long T_2 value.



Diuresis/Antidiuresis Relaxometry

During osmotic diuresis, the urea remains largely in the outer medulla and cortex at the imaging start time used (40 seconds after the beginning of a 12-second injection). During antidiuresis, a larger fraction of the urea is collected in the IM and papilla consistent with UT-A1 and UT-A3 transporter activity. When the acquisition delay allowed for inner medullary urea accumulation, large T_2 increases were observed because of a strong inward T_2 gradient. Supplemental Video 3  shows the

dynamic ^{13}C urea at multiple TE. During antidiuresis, not only is greater inner medullary accumulation of the ^{13}C urea observed but the signal also persists to very late TE.

Figure 4 shows T_2 exponential relaxometry performed with both imaging agents in rats on induced diuresis and antidiuresis. Rather than selecting the short or long T_2 components, the mean (T_2) [calculated in equation (3) with $\alpha = 0.3$ seconds, $\beta = 20$ seconds] was used to simplify analysis. A large (T_2) increase was observed in the IM and renal papilla with ^{13}C , $^{15}\text{N}_2$ urea during antidiuresis (Figure 4A). This (T_2) increase in the kidneys' central region was not observed during diuresis (Figure 4B). The signal distribution and (T_2) of HMCP did not change significantly between antidiuresis and diuresis (Figure 4, A and B, right). In the dynamic HMCP images shown in Supplemental Video 4 , the late TE of the rats during diuresis and antidiuresis look similar. The summary of regional (T_2) measurements from all 3 animals is presented in Figure 4D. Statistically significant (T_2) increases ($P = .001$) were observed with ^{13}C , $^{15}\text{N}_2$ urea in the IM during antidiuresis.

Both agents showed (T_2) lengthening in the IM and papilla. Unlike ^{13}C , $^{15}\text{N}_2$ urea, HMCP showed a small (T_2) reduction in the cortex and outer medulla compared with blood. HMCP had a much higher (T_2) in the vascular pool (3 seconds) compared with urea (1 seconds), which can be seen in the outer margins of the images in Figure 4, A and B, right). With ^{13}C , $^{15}\text{N}_2$ urea, (T_2) values > 2 seconds were only observed within the kidney.

Signal in the ureters could be observed in osmotic diuresis conditions with both ^{13}C , $^{15}\text{N}_2$ urea and HMCP. This can be visualized in the raw images Supplemental Videos 3  and 4 , right panels. After image alignment, denoising, and summing late TE (TE = 7 to 20 seconds), the ureters are more easily visible (Figure 5). The inner lumen of the rat ureter has a diameter between 50 and 150 μm (45), so a 1-mm-wide pixel (acquired in a perpendicular plane to the ureter axis) contains 10 nL of intra-ureter fluid. Although the signal was extremely faint, the persistence of the signal allowed for detectable ureter structure. HMCP had a much stronger signal than ^{13}C , $^{15}\text{N}_2$ urea in the ureters likely because of its longer T_1 . Ureters were only visible in 2 of the 3 diuresis scans for HMCP and 1 of 3 scans for ^{13}C , $^{15}\text{N}_2$ urea.

T_2 -Edited 3D Imaging

Figure 6 shows 3D ^{13}C , $^{15}\text{N}_2$ urea images acquired at 1.2 mm isotropic resolution (1.73 mm^3 pixel volume). These images are

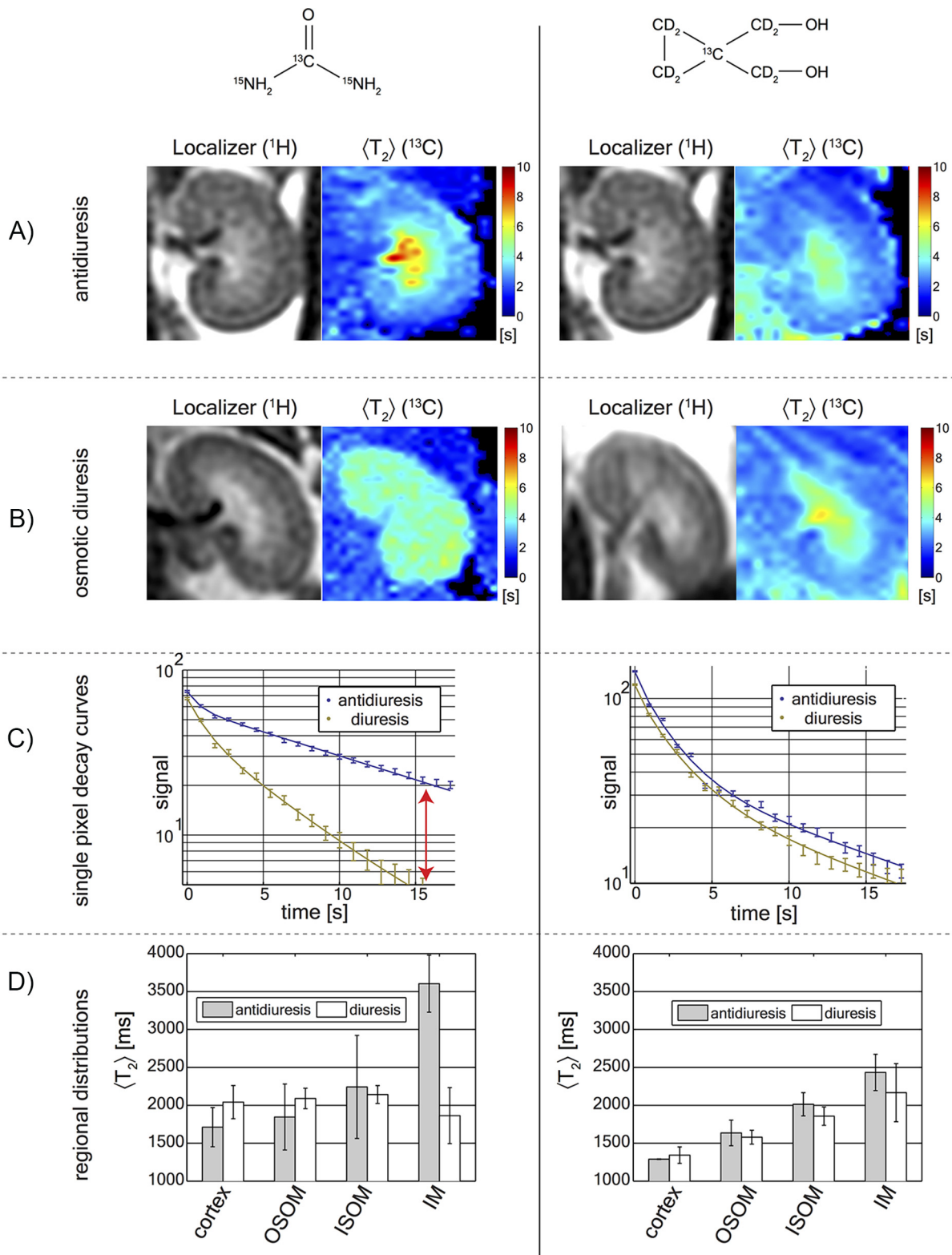


Figure 4. Hyperpolarized [^{13}C , $^{15}\text{N}_2$]urea and HMCP relaxometry during antidiuresis and diuresis. Hyperpolarized [^{13}C , $^{15}\text{N}_2$]urea and HMCP images are shown the left and right columns, respectively. HMCP showed increased medullary T_2 , but the effect did not vary between antidiuresis (A) and diuresis (B) states. Decay curves are selected from a single pixel in the inner medulla (IM) (C). The red arrow shows the persistence of signal to late TE. Mean renal pixel T_2 distributions from 3 animals computed from average values over the cortex, outer stripe of the outer medulla (OSOM), inner stripe of the outer medulla (ISOM), and IM (D). The statistically significant change observed was the [^{13}C , $^{15}\text{N}_2$]urea T_2 in the IM consistent with the urea transporter (UT)-A1 and UT-A3 distribution.

of the blood pool suppression is evidenced by the low background signal and the dark interlobular arteries (magenta arrows on the image panels) and is concordant with the 3- to 5-fold suppression expected from simulation. The OSOM enhanced later than the cortex and ISOM (see the 20- and 25-second time points). Once inner medullary accumulation occurred, the IM and papilla were bright because of the sequence weighting (see simulations in Figure 6A, right). Some residual aliasing is observed from the bright major arteries in the anterior/posterior dimensions, but these artifacts do not interfere substantially with visualization of renal anatomical structures.

DISCUSSION

The minimal attenuation of the long T2 [¹³C, ¹⁵N₂]urea signals by the macromolecular chaser provided strong evidence that these long-T2 signals reside in the extravascular space. The confinement to the kidney further suggests that the long T2 signals represent urea from within the tubular lumen of the nephron, but contribution from the medullary interstitium may have been large. In the nephron segments with high urea permeability, such as the proximal tubule, the thin limbs of the loop of Henle, and the inner medullary collecting ducts (46, 2), urea easily passes through the tubular membrane and enters the interstitial fluid where it then may reenter the blood stream via the peritubular vascular network. The relative contribution of the tubular lumen and interstitium to the long T2 urea signals cannot be

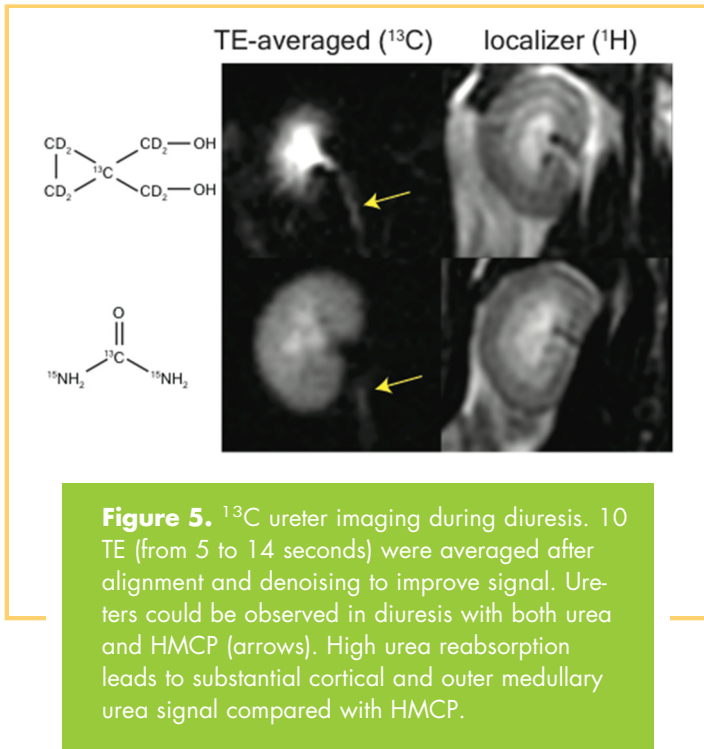
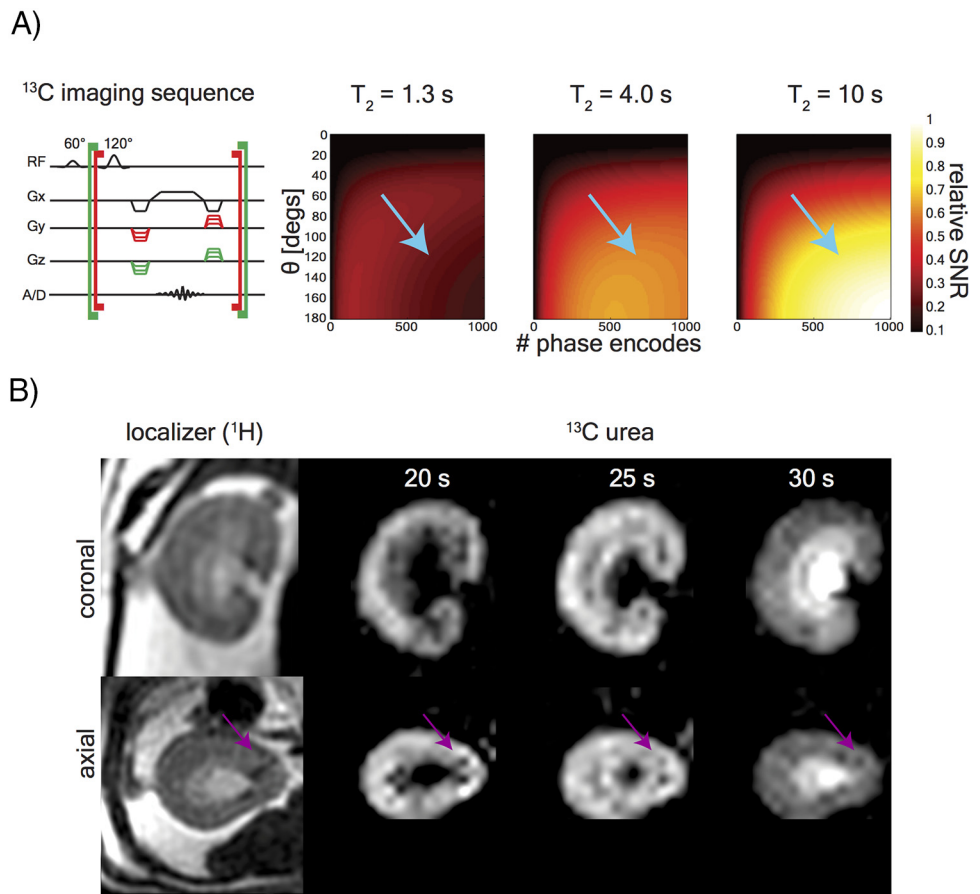


Figure 5. ¹³C ureter imaging during diuresis. 10 TE (from 5 to 14 seconds) were averaged after alignment and denoising to improve signal. Ureters could be observed in diuresis with both urea and HMCP (arrows). High urea reabsorption leads to substantial cortical and outer medullary urea signal compared with HMCP.

zoomed to a single kidney, but the full FOV in all 3 dimensions can be seen in the Supplemental Video 5 [PLAY VIDEO](#). The efficacy

Figure 6. T2-edited 3-dimensional (3D) imaging. Sequence design (left) and signal simulations (right 3 panels) of a 1.7 mm³ isotropic resolution image (A). Simulations show the signal response expected from regions with T₂ = 1.3 seconds (vascular pool), T₂ = 4 seconds (cortex/outer medulla), and T₂ = 10 seconds (IM/papilla). Blue arrows indicate sequence parameters used, and thus the signal response expected in the images. The long effective TE (4 seconds) of a 3D acquisition was used for blood pool signal suppression and for encoding the [¹³C, ¹⁵N₂]urea at 1.2-mm isotropic resolution (B). ¹³C urea images are acquired at 3 different delay times after 3 different injections. Blood pool suppression is evidenced by the dark interlobular arteries visible on both the [¹³C, ¹⁵N₂]urea and ¹H fast spin echo images (magenta arrows).



readily deduced from these data. Urea (mass ~63 Da) and HMCP (mass ~110 Da) are both freely filtered at the glomerulus, but the late TE urea image (Figure 5, bottom left) still shows a substantial cortical signal. Residual cortical signal may signify the relative inefficiency of urea excretion without the aid of the UTs. The increase in the large inner medullary T₂ observed during antidiuresis likely signifies a large interstitial fraction of the [¹³C,¹⁵N₂]urea because vasopressin increases the urea permeability of the inner medullary collecting ducts by 400% (5). Furthermore, micro-computed tomography studies have shown that the blood supply in the IM is sparse and has a vascular volume fraction of <0.2% in rats (47). These observations coincide with a theory that the [¹³C,¹⁵N₂]urea T₂ reports on an effective blood exposure time. Based on measurements in prior studies, [¹³C,¹⁵N₂]urea experiences strong relaxation enhancement in plasma (T₂ = 11 seconds) and whole blood (T₂ = 5 seconds) compared with aqueous solution (T₂ = 24 seconds) (30). Although the strongest in vitro relaxation enhancement was observed in whole blood, this value is more than double of that measured in vivo (T₂ = 1.0 seconds), potentially indicating a large decrease in the apparent T₂ because of the flow. Relaxation enhancement in erythrocytes could be because of a combination of high erythrocyte membrane permeability (48) and lengthened rotational correlation times due to high blood viscosity. Urea erythrocyte permeability is mediated by the erythrocyte isoform of the UT-B. A 20% reduction in the diffusion coefficient of urea has been reported in UT-B-expressed tissue xenografts compared with controls, likely indicating an increased intracellular pool size (13). Controlled experiments in erythrocytes reported changes in the resonant frequency (49) and reduction of the longitudinal T₁ (14) of the intracellular [¹³C]urea. These results are concordant with shortening of the vascular T₂ due to erythrocyte permeability. A recent study by Laustsen et al. noted a very large renal [¹³C,¹⁵N₂]urea T₂ change as a function tissue oxygenation (50), which further supports the hypothesis of a strong relaxation enhancement from the intracellular erythrocyte urea pool, particularly from deoxyhemoglobin. An intriguing finding was that these changes were not observed in diabetic rodent models.

The lack of substantial cortical signals in the HMCP images in Figure 5 suggests that HMCP, similar to GdDTPA (51, 52), may not undergo any significant reabsorption as would be expected from a nonendogenous molecule. It is worth noting that other endogenous molecular probes for hyperpolarized ¹³C MRI such as pyruvate and lactate are also freely filtered but are nearly completely reabsorbed under normal conditions (53, 54). The lack of HMCP (T₂) changes between diuresis and antidiuresis allows for the (T₂) changes observed with [¹³C,¹⁵N₂]urea to be more definitively attributed to the action of urea-specific transporters. This is important because hyperpolarized ¹³C experiments require relatively large contrast agent bolus volumes compared with the total animal blood volume. In each experiment, the rat was given 2 injections of 3 mL of hyperpolarized contrast agents spaced at least 2 hours apart. For the macromolecular relaxation experiments, the rat was given 2 additional injections of 1 mL of Gd contrast. The total injected volume equals ~1/4 the animals' total blood volume and had an unknown effect on cardiac output, GFR, and renal concentrating

capacity. In addition, the urea mixture contained glycerol, which, in large doses, is known to cause a decrease in GFR in rats (55). Although it is difficult to conclude that this large aggregate injection volume had no transient effect on renal function, the apparent independence of HMCP (T₂) measurements on diuresis/antidiuresis states offer imaging-based evidence that the renal concentrating capacity was relatively unchanged with repeat injections when the imaging was started at a constant duration after the injection.

The vascular T₂ of HMCP measured here (T₂ = 4 seconds at B₀ = 3 T) is in agreement with a "worst case" value (T₂ = 1.3 seconds at B₀ = 2.35 T) reported previously using SSFP (21) but is over an order of magnitude higher than in in vivo measurements (T₂ = 0.4 seconds at B₀ = 9.4 T) reported using adiabatic refocusing pulses with surface coils (56). Recent studies report [¹³C,¹⁵N₂]urea T₂ values of 0.5 seconds at B₀ = 9.4 T using a slice-selective, radial fast spin echo, suggesting the need for further study in the dependence of apparent T₂ measurements on B₀, contrast agent uptake in tissue, and acquisition type.

Interestingly, the [¹³C,¹⁵N₂]urea T₁ relaxivity of BSA-Gd-DTPA measured here (3.1 ± 0.4 mM⁻¹s⁻¹ per GdDTPA, B₀ = 3 T) is more than an order of magnitude higher than that reported with gadodiamide and [1-¹³C]pyruvate (0.19 ± 0.01 mM⁻¹s⁻¹, B₀ = 4.7 T) (42). This is likely attributable to the increased relaxivity from the slow correlation time of the macromolecule Gd carrier (57), but it may also signify some preferential binding of urea to albumin.

Some experimental limitations are noted. Multicomponent T₂ relaxometry has well-known difficulties in accurately resolving closely spaced T₂ values at the SNR, scan times, and echo spacing permissible on clinical MRI scanners (39). In this study, the SNR limitation was somewhat exacerbated by the polarization loss from T₁ decay during the long delay periods between injection and imaging necessary for renal contrast agent accumulation. The observed T₂ decay times were significantly longer than those typical of in vivo ¹H MRI, which permitted the coarse temporal sampling required by the single-shot, 1-mm-resolution planar readout. Furthermore, T₂ differences between intra- and extravascular [¹³C,¹⁵N₂]urea differed by a factor of at least 3. Decreasing the resolution would allow finer temporal sampling and increased SNR for the stabilization of T₂ distribution estimation (39). T₂ values less than the sampling time of 910 milliseconds are not expected to be resolved accurately. In nonselective in vivo Carr-Purcell-Meiboom-Gill experiments performed after infusion of hyperpolarized [¹³C,¹⁵N₂]urea with finer temporal sampling (10 milliseconds), we observed approximately 30% of the total signal had a T₂ of 300 milliseconds or less; the origin of this signal remains unknown. In addition, polarization variability will lead to random errors in comparing absolute SNR between experiments. Although prior measurements showed <15% variability in [¹³C,¹⁵N₂]urea polarizations when polarization and transport time are kept consistent (30), this potential random error will almost certainly be minimized with the use of automated transport injectors (58) and magnetically shielded transport pathways (59). Systematic errors may also arise in quantitative T₂ mapping because of transmitter strength miscalibrations when using the transient phase of the SSFP signal. As derived by Scheffler, the exponential decay

envelope of the signal is described by a positive eigenvalue (60), and is shown as follows:

$$\lambda_1 = \frac{1}{2} \left((E_1 - E_2) \cos \theta + \sqrt{4E_1E_2 + (E_1 - E_2)^2 \cos^2 \theta} \right), \quad (5)$$

with $E_1 = e^{-TR/T_1}$, $E_2 = e^{-TR/T_2}$. The transmitter offset may be modeled as $\theta = 180^\circ + \delta\theta$, and a Taylor expansion of λ_1 gives the following equation:

$$\lambda_1 \approx a_0 + a_1 \delta\theta + a_2 \delta\theta^2 + \dots \quad (6)$$

with

$$a_0 = E_2 \quad (7)$$

$$a_1 = 0 \quad (8)$$

$$a_2 = \frac{E_2(E_1 - E_2)}{E_1 + E_2} \quad (9)$$

Nonideal π pulses will cause some apparent lengthening of the measured T2 by introducing some T1 weighting. However, these errors show up only as second- or higher-order terms of $\delta\theta$. The second-order term is minimized when $E_1 \approx E_2$, and this condition is expected to be better approximated in the longer T2 regions. Assuming T2 = 1.5 seconds and T1 = 20 seconds, flip angle errors $\delta\theta/\theta$ up to 20% cause the apparent decay time to differ from T2 by <10%.

Given the importance of urea in the urine concentrating mechanism, high-resolution imaging of renal urea handling could be a powerful tool for the investigation of renal physiology. This imaging technique could be applicable to the monitoring of diuretic drugs that act on UTs (7, 6, 61) or to study the effects of antineoplastic drugs, whose side effects include reduced urea concentrating ability (62). Radiologically, this method could address the inherent difficulty of renal perfusion evaluation on patients with impaired renal function and chronic kidney disease, as virtually all commonly used iodinated computed tomography contrast agents and Gd-based MRI contrast agents pose some hazards of acute renal failure in these patients (63, 64). Although urea clearance is well known to be an inaccurate marker for GFR estimation because of its significant reabsorption (2), ^{13}C urea MRI could provide a qualitative assessment of renal perfusion such as is regularly performed on transplantation candidates, before and after ablation for

renal cell carcinoma, and for the assessment of congenital urological abnormalities (44, 65, 66). All experiments in this study were performed on a clinical MRI scanner using infused urea doses that have been shown to be safe for humans with far advanced renal failure (67). Recent studies have also suggested the use of ^{13}C urea as a biocompatible myocardial perfusion marker (68, 69).

Although T2-weighted imaging has been a standard clinical MRI evaluation for 3 decades (70), only a few studies have investigated T2 contrast for in vivo hyperpolarized ^{13}C agents' imaging (71, 30, 72, 50). In addition to chemical shift (16, 73-77) and diffusion-sensitive (78, 13, 79, 72, 80) imaging techniques, T2 relaxometry could be a very useful tool for probing the microenvironment of hyperpolarized ^{13}C molecules in vivo, as it yields high signals, thus allowing for high-resolution encoding.

Imaging of 2 key steps of the renal urea handling process was enabled by a hyperpolarized ^{13}C relaxometry. Selective quenching of the vascular hyperpolarized ^{13}C signal with a macromolecular relaxation agent revealed that a long-T2 component of the [^{13}C , $^{15}\text{N}_2$]urea signal originated from the renal extravascular space, thus allowing the vascular and filtrate pools of the [^{13}C , $^{15}\text{N}_2$]urea to be distinguished via multiexponential analysis. The T2 response to induced diuresis and antidiuresis was performed with 2 imaging agents: hyperpolarized [^{13}C , $^{15}\text{N}_2$]urea and hyperpolarized bis-1,1-(hydroxymethyl)-1- ^{13}C -cyclopropane- $^2\text{H}_8$ (control agent). During antidiuresis, large T2 increases in the IM and papilla were observed using the former agent only, suggesting that T2 relaxometry may be used to monitor the inner medullary UT-A1- and UT-A3-mediated urea concentrating process. A T2-edited, ultralong TE sequence was developed for sub-2 mm³ resolution 3D encoding of [^{13}C , $^{15}\text{N}_2$]urea in the renal filtrate by exploiting relaxation differences in the vascular and filtrate pools.

Supplemental Materials

Video 1: <http://dx.doi.org/10.18383/j.tom.2016.00127.vid.01>

Video 2: <http://dx.doi.org/10.18383/j.tom.2016.00127.vid.02>

Video 3: <http://dx.doi.org/10.18383/j.tom.2016.00127.vid.03>

Video 4: <http://dx.doi.org/10.18383/j.tom.2016.00127.vid.04>

Video 5: <http://dx.doi.org/10.18383/j.tom.2016.00127.vid.05>

ACKNOWLEDGMENTS

The authors gratefully acknowledged funding from the National Institutes of Health (grants P41EB013598, K01DK099451, NIH/NCI R01CA172845, and R01DK101373), the Surbeck Foundation, and the ARCS foundation.

Disclosure: Dr. Galen Reed reports other from HeartVista, outside the submitted work. He is currently an employee at HeartVista and receives salary support. This work

REFERENCES

- Guyton AC. Renal Regulation of Blood Volume and Extracellular Fluid Volume: Excretion and Regulation of Urea, Potassium, and Other Substances. Textbook of Medical Physiology, Eighth Edition. Philadelphia. W. B. Saunders Company; 1991.
- Marsh DJ, Knepper MA. Renal handling of urea. *Compr Physiol*. 2011; p.1317-1347.
- Bankir L, Yang B. New insights into urea and glucose handling by the kidney, and the urine concentrating mechanism. *Kidney Int*. 2012;81: 1179-1198.
- Fenton RA, Knepper MA. Urea and renal function in the 21st century: insights from knockout mice. *J Am Soc Nephrol*. 2007;18:679-688.
- Sands JM. Regulation of renal urea transporters. *J Am Soc Nephrol*. 1999;10:635-646.
- Yao C, Anderson MO, Zhang J, Yang B, Phuan PW, Verkman AS. Triazolothienopyrimidine inhibitors of urea transporter UT-B reduce urine concentration. *J Am Soc Nephrol*. 2012;23(7):1210-1220.
- Esteva-Font C, Cil O, Phuan PW, Su T, Lee S, Anderson MO, Verkman AS. Diuresis and reduced urinary osmolality in rats produced by small-molecule UT-A-selective urea transport inhibitors. *FASEB J*. 2014;28(9):1-13.

presented here was performed while this author was a graduate student at UCSF.

Conflict of Interest: None reported.

8. Maril N, Margalit R, Mispelterand J, Degani H. Functional sodium magnetic resonance imaging of the intact rat kidney. *Kidney Int.* 2004;65:927–935.
9. Maril N, Rosen Y, Reynolds GH, Ivanishev A, Ngo L, Lenkinski RR. Sodium MRI of the human kidney at 3 Tesla. *Magn Reson Med.* 2006;56(6):1229–1234.
10. Dagher AP, Aletas A, Choyke P, Balaban RS. Imaging of urea using chemical exchange-dependent saturation transfer at 1.5 T. *J Magn Reson Imaging.* 2000;12(5).
11. Golman K, Ardenkjær-Larsen JH, Petersson JS, Mansson S, Leunbach Ib. Molecular imaging with endogenous substances. *Proc Natl Acad Sci U S A.* 2003;100(18):10435–10439.
12. von Morze C, Bok RA, Sands JM, Kurhanewicz J, Vigneron DB. Monitoring urea transport in rat kidney in vivo using hyperpolarized ¹³C magnetic resonance imaging. *Am J Physiol Renal Physiol.* 2012;302(12):F1658–F1662.
13. Patrick PS, Kettunen MI, Tee SS, Rodrigues TB, Serrao E, Timm KN, McGuire S, Brindle KM. Detection of transgene expression using hyperpolarized ¹³C urea and diffusion weighted magnetic resonance spectroscopy. *Magn Reson Med.* 2015;73(4):1401–1406.
14. Páges G, Puckeridge M, Liangfeng G, Tan YL, Jacob C, Garland M, Kuchel PW. Transmembrane exchange of hyperpolarized ¹³C-urea in human erythrocytes: subminute timescale kinetic analysis. *Biophys J.* 2013;105(9):1956–1966.
15. von Morze C, Larson PEZ, Hu S, Keshari K, Wilson DM, Ardenkjær-Larsen JH, et al. Imaging of blood flow using hyperpolarized [(13)C]urea in preclinical cancer models. *J Magn Reson Imaging.* 2011;33(3):692–697.
16. Golman K, Zandt R, Thaning M. Real-time metabolic imaging. *Proc Natl Acad Sci U S A.* 2006;103(30):11270–11275.
17. Golman K, Zandt R, Lerche M, Pehrson R, Ardenkjær-Larsen JH. Metabolic imaging by hyperpolarized ¹³C magnetic resonance imaging for in vivo tumor diagnosis. *Cancer Res.* 2006;66(22):10855–10860.
18. Keshari KR, Wilson DM. Chemistry and biochemistry of ¹³C hyperpolarized magnetic resonance using dynamic nuclear polarization. *Chem Soc Rev.* 2014;43(5):1627–1659.
19. Claiworthy MR, Kettunen MI, Hu DE, Mathews RJ, Witney TH, Kennedy BWC, et al. Magnetic resonance imaging with hyperpolarized 1,4-¹³C₂fumarate allows detection of early renal acute tubular necrosis. *Proc Natl Acad Sci U S A.* 2012;109(33):13374–13379.
20. Grant AK, Vinogradov E, Wang X, Lenkinski RE, Alsop DC. Perfusion imaging with a freely diffusible hyperpolarized contrast agent. *Magn Reson Med.* 2011;66(3):746–755.
21. Svensson J, Mansson S, Johansson E, Petersson JS, Olsson LE. Hyperpolarized ¹³C MR angiography using TrueFISP. *Magn Reson Med.* 2003;50(2):256–262.
22. Merritt ME, Harrison C, Storey C, Jeffrey FM, Sherry AD, Malloy CR. Hyperpolarized ¹³C allows a direct measure of flux through a single enzyme-catalyzed step by NMR. *Proc Natl Acad Sci U S A.* 2007;104(50):19773–19777.
23. Laustsen C, Lycke S, Palm F, Østergaard JA, Kirby BM, Nørregaard R, Flyvbjerg A, Pedersen M, Ardenkjær-Larsen JH. High altitude may alter oxygen availability and renal metabolism in diabetics as measured by hyperpolarized [1-(13)C]pyruvate magnetic resonance imaging. *Kidney Int.* 2014;86:67–74.
24. Keshari KR, Kurhanewicz J, Bok R, Larson PEZ, Vigneron DB, Wilson DM. Hyperpolarized ¹³C dehydroascorbate as an endogenous redox sensor for in vivo metabolic imaging. *Proc Natl Acad Sci U S A.* 2011;108(46):18606–18611.
25. Keshari KR, Wilson DM, Chen AP, Bok R, Larson PEZ, Hu S, Van Criekinge M, Macdonald JM, Vigneron DB, Kurhanewicz J. Hyperpolarized [2-¹³C]-fructose: a hemiketal DNP substrate for in vivo metabolic imaging. *J Am Chem Soc.* 2009;131(48):17591–17596.
26. Keshari KR, Kurhanewicz J, Macdonald JM, Wilson DM. Generating contrast in hyperpolarized ¹³C MRI using ligand-receptor interactions. *Analyst.* 2012;137(15):3427–3429.
27. Ardenkjær-Larsen JH, Fridlund B, Gram A, Hansson G, Hansson L, Lerche MH, Servin R, Thaning M, Golman K. Increase in signal-to-noise ratio of > 10,000 times in liquid-state NMR. *Proc Natl Acad Sci U S A.* 2003;100(18):10158–10163.
28. Chattergoon N, Martinez-Santesteban F, Handler WB, Ardenkjær-Larsen JH, Scholl TJ. Field dependence of T1 for hyperpolarized 1-¹³C pyruvate. *Contrast Media Mol Imaging.* 2013;8(1):57–62.
29. Golman K, Axelsson O, Johannesson H, Mansson S, Olofsson C, Petersson JS. Parahydrogen-induced polarization in imaging: subsecond (13)C angiography. *Magn Reson Med.* 2001;46(1):1–5.
30. Reed GD, von Morze C, Bok R, Koelsch BL, Smith KJ, Shang H, et al. High resolution (13)C MRI with hyperpolarized urea: in vivo T(2) mapping and (15)N labeling effects. *IEEE T Med Imaging.* 2014;33(2):362–371.
31. Kokko JP, Rector FC Jr. Countercurrent multiplication system without active transport in the inner medulla. *Kidney Int.* 1972;2(4):85–94.
32. von Morze C, Bok RA, Reed GD, Ardenkjær-Larsen JH, Kurhanewicz J, Vigneron DB. Simultaneous multiagent hyperpolarized ¹³C perfusion imaging. *Magn Reson Med.* 2014;72(6):1599–1609.
33. Chiavazza E, Kubala E, Gringeri CV, Duwel S, Durst M, Schulte RF, Menzel MI. Earth's magnetic field enabled scalar coupling relaxation of ¹³C nuclei bound to fast-relaxing quadrupolar ¹⁴N in amide groups. *J Magn Reson.* 2013;227:35–38.
34. Ogan MD, Schmiel U, Moseley ME, Grodd W, Paaanen H, Brasch RC. Albumin labeled with Gd-DTPA. An intravascular contrast-enhancing agent for magnetic resonance blood pool imaging: preparation and characterization. *Invest Radiol.* 1987;22(8):665–671.
35. Dafni H, Larson PEZ, Hu S, Yoshihara HAI, Ward CS, Venkatesh HS, et al. Hyperpolarized ¹³C spectroscopic imaging informs on hypoxia-inducible factor-1 and myc activity downstream of platelet-derived growth factor receptor. *Cancer Res.* 2010;70(19):7400–7410.
36. Jha SK, Yadava RDS. Denoising by singular value decomposition and its application to electronic nose data processing. *IEEE Sens J.* 2011;11(1):35–44.
37. Provencher SW. An eigenfunction expansion method for the analysis of exponential decay curves. *J Chem Phys.* 1976;64:2772–2777.
38. Whittall KP, MacKay AL. Quantitative interpretation of NMR relaxation data. *J Magn Reson.* 1989;84(1):134–152.
39. Graham SJ, Stanchev PL, Bronskill MJ. Criteria for analysis of multi compartment tissue T2 relaxation data. *Magn Reson Med.* 1996;35:370–378.
40. Raj A, Pandya S, Shen X, LoCastro E, Nguyen TD, Gauthier SA. Multi-compartment T2 relaxometry using a spatially constrained multi-Gaussian model. *PLoS One.* 2014;9(6):e98391.
41. Kim SJ, Koh K, Lustig M, Boyd S. An interior point method for large-scale ℓ_1 -regularized least squares. *IEEE J Sel Topics Signal Process.* 2007;1(4):606–617.
42. Smith MR, Peterson ET, Gordon JW, Niles DJ, Rowland U, Kurpad KN, Fain SB. In vivo imaging and spectroscopy of dynamic metabolism using simultaneous ¹³C and ¹H MRI. *IEEE Trans Biomed Eng.* 2012;59(1):45–49.
43. Lee HB, Blafox MD. Blood Volume in the Rat. *J Nucl Med.* 1985;26(1):72–76.
44. Zhang JL, Morrell G, Rusinek H, Sigmund EE, Chandarana H, Lerman LO, Prasad PV, Niles D, Artz N, Fain S, Vivier PH, Cheung AK, Lee VS. New magnetic resonance imaging methods in nephrology. *Kidney Int.* 2014;85(4):768–779.
45. Hicks RM. The fine structure of the transitional epithelium of rat ureter. *J Cell Biol.* 1965;26(1):25–48.
46. Lassiter WE, Gottschalk CW, Mylle M. Micropuncture study of net transtubular movement of water and urea in nondiuretic mammalian kidney. *Am J Physiol.* 1961;200:1139–1147.
47. Garcia-Sainz A, Rodriguez-Barbero A, Bentley MD, Ritman EE, Romero JC. Three-dimensional microcomputed tomography of renal vasculature in rats. *Hypertension.* 1998;31(1 Pt 2):440–444.
48. Brahm J. Urea permeability of human red cells. *J Gen Physiol.* 1983;82(1):1–23.
49. Potts JR, Bulliman BT, Kuchel PW. Urea exchange across the human erythrocyte membrane measured using ¹³C NMR lineshape analysis. *Eur Biophys J.* 1992;21(3):207–216.
50. Laustsen C, Nørting TS, Hansen DC, Qi H, Nielsen PM, Bertelsen LB, Ardenkjær-Larsen JH, Jørgensen HS. Hyperpolarized ¹³C urea relaxation mechanism reveals renal changes in diabetic nephropathy. *Magn Reson Med.* 2016;75(2):515–518.
51. Choyke PL, Frank JA, Girton ME, Inscoe SW, Carvlin MJ, Black JL, Austin HA, Dwyer AJ. Dynamic Gd-DTPA-enhanced MR imaging of the kidney: experimental results. *Radiology.* 1989;170(3 Pt 1):713–720.
52. Lee VS, Rusinek H, Bokacheva L, Huang AJ, Oesingmann N, Chen Q, Kaur M, Prince K, Song T, Kramer EL, Leonard EF. Renal function measurements from MR renography and a simplified multicompartmental model. *Am J Physiol Renal Physiol.* 2007;292(5):F1548–F1559.
53. Hohmann B, Frohnert PP, Kinne R, Baumann K. Proximal tubular lactate transport in rat kidney: A micropuncture study. *Kidney Int.* 1974;5(4):261–270.
54. Anderson J, Marks V. Pyruvate in diabetes mellitus concentrations in urine and blood. *Lancet.* 1962;1(7240):1159–1161.
55. Lin JH, Lin TH. Renal handling of drugs in renal failure. I: Differential effects of uranyl nitrate- and glycerol-induced acute renal failure on renal excretion of TEAB and PAH in rats. *J Pharmacol Exp Ther.* 1988;246(3):896–901.
56. Kettunen MI, Kennedy BWC, Hu D, Brindle KM. Spin echo measurements of the extravasation and tumor cell uptake of hyperpolarized [1-(13)C]lactate and [1-(13)C]pyruvate. *Magn Reson Med.* 2013;70(5):1200–1209.
57. Werner EJ, Datta A, Jocher CJ, Raymond KN. High-relaxivity MRI contrast agents: where coordination chemistry meets medical imaging. *Angew Chem Int Ed Engl.* 2008;47(45):8568–8580.
58. Cheng T, Mishkovsky M, Bastiaansen JA, Ouari O, Haulte P, Tordo P, van den Brandt B, Comment A. Automated transfer and injection of hyperpolarized molecules with polarization measurement prior to in vivo NMR. *NMR Biomed.* 2013;26(11):1582–1588.
59. Milani J, Vuichoud B, Bornet A, Mieville P, Mottier R, Jannin S, Bodenhausen G. A magnetic tunnel to shelter hyperpolarized fluids. *Rev Sci Instrum.* 2015;86(2):024101.
60. Scheffler K. On the transient phase of balanced SSFP sequences. *Magn Reson Med.* 2003;43(4):781–783.

61. Sands JM. Urea transporter inhibitors: en route to new diuretics. *Chem Biol.* 2013;20(10):1201–1202.
62. Safirstein R, Miller P, Dikman S, Lyman N, Shapiro C. Cisplatin nephrotoxicity in rats: defect in papillary hypertonicity. *Am J Physiol.* 1981;241(2):F175–F185.
63. Parfrey PS, Griffiths SM, Barrett BJ, Paul MD, Genge M, Withers J, Farid N, McManamon PJ. Contrast material-induced renal failure in patients with diabetes mellitus, renal insufficiency, or both. *N Engl J Med.* 1989;320(3):143–149.
64. Morcos SK. Contrast media-induced nephrotoxicity—questions and answers. *Br J Radiol.* 1998;71(844):357–365.
65. Gervais DA, McGovern FJ, Arellano RS, McDougal WS, Mueller PR. Radiofrequency ablation of renal cell carcinoma: part 1, Indications, results, and role in patient management over a 6-year period and ablation of 100 tumors. *AJR Am J Roentgenol.* 2005;185(1):64–71.
66. Prasad PV. Functional MRI of the kidney: tools for translational studies of pathophysiology of renal disease. *Am J Physiol Renal Physiol.* 2006;290(5):F958–F974.
67. Johnson W, Hagge W, Wagoner R, Dinapoli R, Rosevear J. Effects of urea loading in patients with far-advanced renal failure. *Mayo Clin Proc.* 1972;47(1):21–29.
68. Lau AZ, Miller JJ, Robson MD, Tyler DJ. Cardiac perfusion imaging using hyperpolarized ^{13}C urea using flow sensitizing gradients. *Magn Reson Med.* 2016;75(4):1474–1483. [Epub 2015 May 20]
69. Lau AZ, Miller JJ, Robson MD, Tyler DJ. Simultaneous assessment of cardiac metabolism and perfusion using copolarized $[1-^{13}\text{C}]$ pyruvate and ^{13}C -urea. *Magn Reson Med.* 2016. doi: 10.1002/mrm.26106. [Epub ahead of print].
70. Hennig J, Nauerth A, Friedburg H. RARE imaging: a fast imaging method for clinical MR. *Magn Reson Med.* 1986;3(6):823–833.
71. Yen YF, Le Roux P, Mayer D, King R, Spielman D, Tropp J, Pauly KB, Pfefferbaum A, Vasanawala S, and Hurd R. T2 relaxation times of ^{13}C metabolites in a rat hepatocellular carcinoma model measured in vivo using ^{13}C -MRS of hyperpolarized $[1-^{13}\text{C}]$ pyruvate. *NMR Biomed.* 2010;23(4):414–423.
72. Kettunen MI, Kennedy BWC, Hu De, Brindle KM. Spin echo measurements of the extravasation and tumor cell uptake of hyperpolarized $[1-^{13}\text{C}]$ lactate and $[1-^{13}\text{C}]$ pyruvate. *Magn Reson Med.* 2013;70(5):1200–1209.
73. Witney TH, Kettunen MI, Brindle KM. Kinetic modeling of hyperpolarized ^{13}C label exchange between pyruvate and lactate in tumor cells. *J Biol Chem.* 2011;286(28):24572–24580.
74. Schulte RF, Sperl JJ, Weidl E, Menzel MI, Janich MA, Khagai O, Durst M, Ardenkjaer-Larsen JH, Glaser SJ, Haase A, Schwaiger M, Wiesinger F. Saturation-recovery metabolic-exchange rate imaging with hyperpolarized $[1-^{13}\text{C}]$ pyruvate using spectral-spatial excitation. *Magn Reson Med.* 2013;69(5):1209–1216.
75. Josan S, Yen YF, Hurd R, Pfefferbaum A, Spielman D, Mayer D. Application of double spin echo spiral chemical shift imaging to rapid metabolic mapping of hyperpolarized $[1-^{13}\text{C}]$ -pyruvate. *J Magn Reson.* 2011;209(2):332–336.
76. Lau AZ, Chen AP, Ghugre NR, Ramanan V, Lam WW, Connelly KA, Wright GA, Cunningham CH. Rapid multislice imaging of hyperpolarized ^{13}C pyruvate and bicarbonate in the heart. *Magn Reson Med.* 2010;64(5):1323–1331.
77. Ramirez MS, Lee J, Walker CM, Sandulache VC, Hennel F, Lai SY, Bankson JA. Radial spectroscopic MRI of hyperpolarized $[1-^{13}\text{C}]$ pyruvate at 7 tesla. *Magn Reson Med.* 2014;72(4):986–995.
78. Koelsch BL, Reed GD, Keshari KR, Chaumeil MM, Bok R, Ronen SM, Vigneron DB, Kurhanewicz J, Larson PE. Rapid in vivo apparent diffusion coefficient mapping of hyperpolarized ^{13}C metabolites. *Magn Reson Med.* 2015;74(3):622–633.
79. Larson PEZ, Kerr AB, Reed GD, Hurd RE, Kurhanewicz J, Pauly JM, Vigneron DB. Generating super stimulated-echoes in MRI and their application to hyperpolarized C-13 diffusion metabolic imaging. *IEEE Trans Med Imaging.* 2012;31(2):265–275.
80. Schilling F, Duwel S, Kollisch U, Durst M, Schulte RF, Glaser SJ, Haase A, Otto AM, Menzel MI. Diffusion of hyperpolarized ^{13}C -metabolites in tumor cell spheroids using real-time NMR spectroscopy. *NMR Biomed.* 2013;26(5):557–568.